


RESEARCH ARTICLE OPEN ACCESS

Self-Catalyzed AlGaAs Nanowires and AlGaAs/GaAs Axial Heterostructures Grown by Molecular Beam Epitaxy

Giorgos Boras¹  | Haotian Zeng¹ | Stephen Church² | Raghavendra Juluri³ | Anton Velichko⁴ | Huiwen Deng¹ | Hui Jia¹ | Francisco Alvarado³ | Ziyue Yin¹ | Chong Chen¹ | Jaeseong Park¹ | Mingchu Tang¹ | David Mowbray⁴ | Ana M. Sanchez³ | Patrick Parkinson² | Huiyun Liu¹

¹Department of Electronic and Electrical Engineering, University College London, London, UK | ²Department of Physics and Astronomy and the Photon Science Institute, University of Manchester, Manchester, UK | ³Department of Physics, University of Warwick, Coventry, UK | ⁴School School of Physics and Astronomy, University of Sheffield, Sheffield, UK

Correspondence: Giorgos Boras (uceegbo@ucl.ac.uk) | Haotian Zeng (haotian.zeng.13@ucl.ac.uk)

Received: 10 October 2025 | **Revised:** 10 November 2025 | **Accepted:** 19 November 2025

Keywords: AlGaAs | branches | growth control | nanowire quantum dots | nanowires | ternary

ABSTRACT

Self-catalyzed AlGaAs nanowires (NWs) offer advantageous properties, including lattice matching to GaAs, a wide range of electronic bandgaps, and monolithic integration with the mature Si platform due to elastic strain relaxation. However, the growth of self-catalyzed AlGaAs NWs is typically characterized by morphological challenges, such as branching and tapering. Here, we comprehensively investigate the optimization of the group III growth rate and V/III ratio. We demonstrate the growth of AlGaAs NWs using a Ga/Al alloy droplet as a co-catalyst, achieving minimal branching and NW uniformity with up to 40% nominal Al content. Embedding a single GaAs segment in an optimized NW structure results in QD-like properties, including strong spatially localized emission at room temperature. Our findings demonstrate the control of branching events in self-catalyzed AlGaAs NWs, highlighting their potential for applications including nanolasers and quantum light emitters.

1 | Introduction

III-V semiconductor nanowires (NWs) are important candidates for next-generation optoelectronics and Si photonics due to their direct bandgap and ease of monolithic integration with Si [1, 2]. Among the various classes of materials used, ternary alloys are particularly promising owing to their tunable bandgap and high degree of structural design freedom [3, 4].

The AlGaAs platform is lattice-matched to GaAs, enabling virtually strain-free AlGaAs/GaAs heterostructures [5]. Hence, GaAs/AlGaAs has been employed in core/shell NWs for nanolasers [6–8], light-emitting diodes (LEDs) [9, 10], and

photodetectors [11, 12], while GaAs quantum dots (QDs) in AlGaAs NW shells show promise as quantum light emitters [13–15]. Despite this interest, the use of AlGaAs NW cores, as opposed to GaAs, is significantly less explored. Using a radial shell of GaAs/AlGaAs quantum wells (QWs) surrounding an AlGaAs NW core could improve lasing performance, as a narrow bandgap GaAs core can absorb lasing photons emitted by the QWs. In addition, the low bandgap of the GaAs core may act as a carrier sink [16–18]. AlGaAs NW cores can host spatially localized axial GaAs QDs for single photon generation, a key requirement in quantum computing systems [19–21]. Despite the challenges associated with the sharpness of the interfaces, good photon antibunching has been reported in Au-catalyzed GaAs/AlGaAs dot-in-wires [19–21]. Moreover, it has been shown

Haotian Zeng and Giorgos Boras contributed equally to this work.

This is an open access article under the terms of the [Creative Commons Attribution](https://creativecommons.org/licenses/by/4.0/) License, which permits use, distribution and reproduction in any medium, provided the original work is properly cited.

© 2025 The Author(s). *Advanced Materials Interfaces* published by Wiley-VCH GmbH

that a GaAs QD displays different properties depending on the crystallinity of the AlGaAs barrier [22], further indicating the importance of the AlGaAs NW core design for a wide range of applications.

To date, AlGaAs NWs have typically used the Au-catalyzed vapor-liquid-solid (VLS) growth mode [23–27]. Utilizing this approach, standing structures have been synthesized with near-infrared emission and with the potential for high electron mobility transistors [23]. Au-catalyzed single GaAs/AlGaAs dot-in-wires have been realized, with narrow emission of 458 μeV at 6 K [24]. Despite these achievements, challenges remain with respect to NW morphology. First, strong tapering is frequently encountered [25–28]. This tapering can enhance light coupling efficiency, due to the adiabatic expansion of the optical mode into air and exciton diffusion to the NW tip [29]; however, the lack of uniformity can hinder device repeatability. In addition, despite the chemical inertness of Au, as a fast-diffusing metal, it can form deep trap states [30], while its ex situ removal increases the complexity of device fabrication. These issues reduce the yield of the Au-catalyzed approach, and a viable alternative method with efficient scalability is required to circumvent these obstacles.

An alternative approach to AlGaAs NW synthesis is the self-catalyzed VLS method, where growth is initiated by an Al/Ga alloy droplet which can be consumed upon growth termination, in situ under high As flux. It has been shown that the optoelectronic properties of self-catalyzed GaAs/AlGaAs core/shell NWs are enhanced when compared to their Au-catalyzed counterparts [31, 32]. Specifically, the latter exhibit poorer minority carrier lifetimes, and their internal quantum efficiency is drastically reduced due to thermally activated Au-induced trap states [32]. In contrast, the performance of self-catalyzed GaAs/AlGaAs NWs has been shown to be comparable to state-of-the-art planar devices [31]. Recently, we demonstrated the synthesis of self-catalyzed AlGaAs core NWs with novel morphological features [33, 34], where the NWs adopt a tree-like configuration via the nucleation of branches perpendicular to the NW trunk [34]. Single GaAs/AlGaAs dot-in-wires have been realized with excellent emission properties, including spatially localized emission and narrow emission linewidths at cryogenic temperatures [33]. These branched NWs are excellent candidates for energy storage applications, for example, solar cells and supercapacitors [35]. However, their morphology can be challenging in terms of light extraction efficiency, which can compromise the GaAs QD emission, especially in structures with increased Al composition where branching is more pronounced [33, 34]. A high ternary alloy Al composition is desirable as it enhances carrier confinement in structures where AlGaAs is used as the barrier, for example, in GaAs/AlGaAs NWQW and NWQD structures [13–15, 30, 33]. Hence, reducing branching while maintaining a high Al composition is an important goal of current AlGaAs NW growth techniques.

In this paper, we report the growth of AlGaAs core NWs via the self-catalyzed approach using molecular beam epitaxy (MBE), realizing branchless AlGaAs NWs with 40% nominal Al composition on Si substrates. We demonstrate the control of branching events with a systematic study of the geometry of the NWs as a function of growth parameters: Ga growth rate, Al composition, and V/III ratio, with structural characteristics

studied using transmission electron microscopy (TEM). We show that the Ga growth rate is crucial for branch formation, with higher growth rates leading to a pronounced branched geometry, while smaller growth rates enable fully branchless structures, even at Al compositions up to 30%. However, high Al composition is still found to promote branching, as observed previously [33, 34]. Optimized growth parameters are used to embed a short single GaAs segment on-axis in an NW with a nominal 40% Al composition. The GaAs emission shows strong spatial localization and saturation at high excitation powers, consistent with band-filling effects due to a reduced density of states (DOS), indicating a reduced dimensionality of the GaAs segment. This result demonstrates the importance of achieving control of the AlGaAs NW morphology and the suitability of branchless AlGaAs NWs with up to 40% Al composition as a host for non-classical light-emitters.

2 | Results and Discussion

To study the influence of growth parameters on the NW morphology, 7 different samples were synthesized, modifying three parameters: Ga growth rate, Al content, and V/III ratio. The categorization of the samples into subsets, the growth parameters used, and the measured dimensions of each structure are shown in Table 1. A structure with a Ga growth rate of 0.4 ML/s, 40% Al content, and a V/III ratio of 20 was selected as the host for a single GaAs segment (indicated in red text in the table), the optical properties of which are studied in detail below.

The as-grown AlGaAs NW morphology was investigated using SEM. As a result of the 4° offcut orientation of the Si substrates, the NWs exhibit a slight tilt with respect to the substrate surface; however, their main elongation is along the $\langle 111 \rangle_B$ direction. The impact of Ga growth rate was assessed via study of sample subset A. SEM images are shown in Figure 1a–c. A low Ga growth rate is observed to promote the synthesis of NWs perpendicular to the Si substrate (Figure 1a) with minimal branching. However, the NWs are short with an average length of 3.8 μm . An increased Ga growth rate of 0.4 ML/s results in longer NWs with an average length of 6.8 μm . These NWs still exhibit mainly trunk-only growth, with only occasional branching observed (Figure 1b). Note that the length of the branches remains short and cannot always be observed due to the resolution limit of the SEM. Finally, the highest Ga growth rate of 0.6 ML/s leads to irregular morphologies, with multiple and pronounced branching events (Figure 1c). These observations indicate control of branch synthesis via the Ga growth rate.

High Al content has been previously associated with extensive branching [33] and pronounced NW tapering; however, high Al content is key for high quantum confinement in cases where AlGaAs is used as the nanostructure barrier material. In sample subset B, the Ga growth rate was kept constant at 0.4 ML/s, and the Al content varied from 20% to 40%. Figure 1d shows a representative SEM image of a sample with 20% Al, where there are no noticeable branches. Increasing the Al composition to 30% still results in most of the NWs maintaining minimal branching (Figure 1e). Finally, for the highest Al content used, i.e., 40%, the NWs maintain a largely uniform morphology but with a few branches being formed. For the NWs with 20%,

TABLE 1 | Growth parameters of the AlGaAs core NWs. The table includes statistics on the NW length and diameter for each structure. The structure indicated with red text was used as the host for a short GaAs segment in a subsequent sample growth. Note that samples A2 and B2, as well as samples B3 and C2, are grown under nominally identical conditions.

| Sample batch | Varying parameter | Sample Code | Ga growth rate (ML/s) | Al content | V/III ratio | Length (μm) | Diameter (nm) |
|--------------|-------------------|-------------|-----------------------|------------|-------------|--------------------------|---------------|
| A | Ga growth rate | A1 | 0.3 | 30% | 20 | 3.8 ± 0.6 | 138 ± 12 |
| | | A2 | 0.4 | | | 6.8 ± 0.4 | 162 ± 17 |
| | | A3 | 0.6 | | | 12.2 ± 1 | 278 ± 24 |
| B | Al content | B1 | 0.4 | 20% | 20 | 6.6 ± 1 | 124 ± 13 |
| | | B2 | | 30% | | 6.8 ± 0.4 | 162 ± 17 |
| | | B3 | | 40% | | 7.2 ± 0.2 | 178 ± 12 |
| C | V/III ratio | C1 | 0.4 | 40% | 15 | 4.6 ± 0.2 | 198 ± 10 |
| | | C2 | | | 20 | 7.2 ± 0.2 | 178 ± 12 |
| | | C3 | | | 25 | 6 ± 0.3 | 180 ± 18 |

30% and 40% Al content, the average lengths are similar: 6.6, 6.8, and 7.2 μm , respectively. The corresponding diameters are approximately 125, 160, and 180 nm, respectively. Based on these observed dimensions, it is proposed that Al is preferably incorporated on the side walls of the NW and hence participates mainly in the radial NW growth, while only a minority of Al adatoms contribute to the axial NW growth. Therefore, despite the synergic influence of Ga growth rate and Al composition on the synthesis of branched NWs, the structures can maintain a uniform morphology with minimal branching even at high Al compositions via a suitable choice of the Ga growth rate.

The effect of varying the V/III ratio on NW morphology was studied in sample subset C, where the Ga growth rate was kept constant at 0.4 ML/s for a constant 40% Al content but with the V/III ratio varying from 15 to 25 (Figure 1g–i). A low V/III ratio of 15 (Figure 1g) leads to a poor morphology, with frequent kinking and branching. This results from the growth dynamics, as the adhesion of Al to the NW sidewalls, as shown in the study of sample subset B, leads to the axial growth being dominated by Ga and As. Hence, a low As flux results in less pronounced axial elongation, leading to morphological roughness, distortions in the NW growth direction, and branching [33]. Increasing the V/III ratio to 20 results in NWs formed approximately perpendicular to the surface and with minimal branching (Figure 1h). The length of the NWs is increased as changes in the growth direction are reduced. Further increase of the V/III ratio to 25 leads to a dramatically decreased NW density as most of the NW growth is suppressed due to rapid Ga droplet consumption under high group V flux (Figure 1i). The current SEM analysis hence demonstrates that control of the AlGaAs NW morphology, particularly the frequency of branching events, can be achieved via the synergic modulation of the three investigated growth parameters.

We conclude that both Ga growth rate and Al composition contribute to the branching events and also NW tapering, potentially allowing the attainment of fully branchless and constant diameter NWs via a careful selection of growth parameters. These findings are supported by our proposed growth mechanism, which is

further discussed in Section 1 of the Electronic [Supplementary Material](#) (ESM).

TEM characterization was conducted to further study the NW structures. Given the improved morphology of the samples with a Ga growth rate of 0.4 ML/s and a V/III ratio of 20, NWs grown under these conditions were selected for TEM study. One representative AlGaAs NW sample with 40% nominal Al content is presented in Figure 2. No branches are observed, as revealed in the bright field (BF) image of Figure 2a. The NW also exhibits good uniformity along its length. The crystal structure was further analyzed by recording high-resolution images for different areas along the length of the NW. A predominantly zinc-blende (ZB) crystal phase with rotational twins is observed in the area enclosed by the blue square (Figure 2b). This is consistent with results previously reported for self-catalyzed AlGaAs NWs [33, 34]. A high density of stacking faults is observed in the area indicated by the green square (Figure 2c). These two types of planar defects, namely twins and stacking faults, are frequently encountered in NWs. Although the NW structure is predominantly ZB, wurtzite (WZ) insertions are observed in the region indicated by the red square (Figure 2d), where a long WZ segment of 250 nm length is present. The high density of defects in the vicinity of the NW tip (Figure 2d) is attributed to the consumption of the Ga droplet under As-rich conditions; more details can be found in the “Growth Methods” section of the current paper. A similar analysis was carried out for NWs with 20% and 30% Al composition and branches that are occasionally observed in a minority of NWs from the 40% Al-containing sample. Details of the analysis of these TEM results can be found in Section 2 of the ESM. The detailed TEM analysis, thus, reveals a ZB crystal structure with the presence of twinning, stacking faults, and WZ segments as the NW growth progresses.

BF images were taken for each sample of subset B, with varying Al content. For each of these samples, 15 individual NWs were studied. Figure 3a corresponds to an NW with 20% Al composition. The structure exhibits no branches consistent with the SEM analysis. Figure 3b shows the morphology of a branchless NW with 30% Al content, while Figure 3c exhibits the same result on

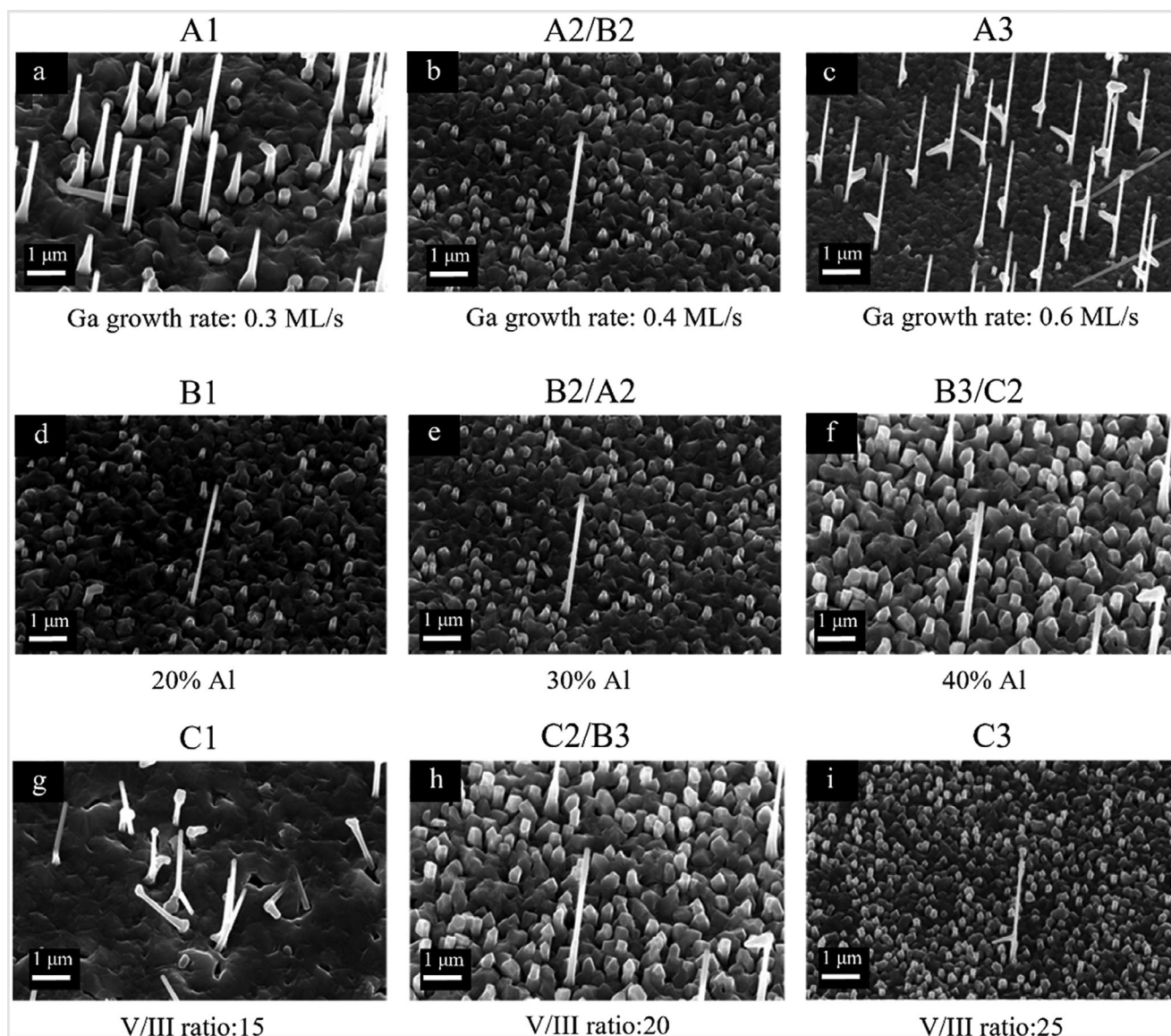


FIGURE 1 | a–c) SEM images of samples of subset A with varying Ga growth rates of 0.3, 0.4, and 0.6 ML/s, respectively. d–f) SEM images of samples of subset B with varying nominal Al compositions of 20%, 30% and 40%, respectively. g–i) SEM images of samples of subset C with varying V/III ratios of 15, 20, and 25, respectively.

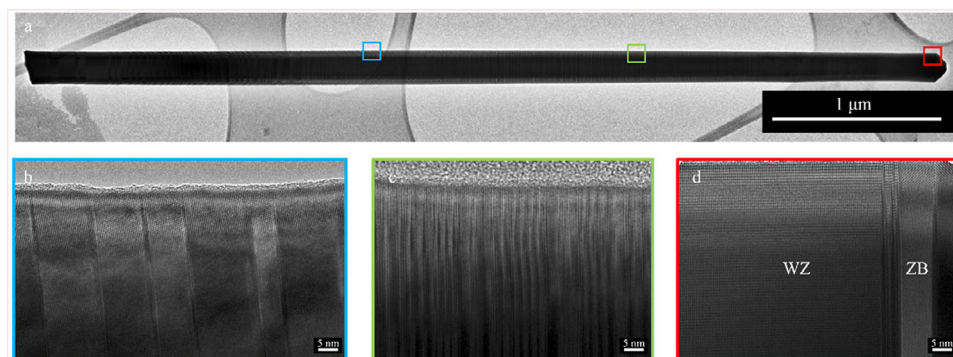


FIGURE 2 | a) Bright Field (BF) TEM image of an AlGaAs NW with 40% nominal Al composition. No branching is observed, with minimal tapering that occurs only at the very tip of the NW. b–d) High-Resolution TEM images corresponding to the areas enclosed in the blue, green, and red squares in a), respectively. Twinning and stacking faults are the main features observed in (b) and (c), respectively. A 250 nm-long WZ insertion is seen in the vicinity of the NW tip in (d).

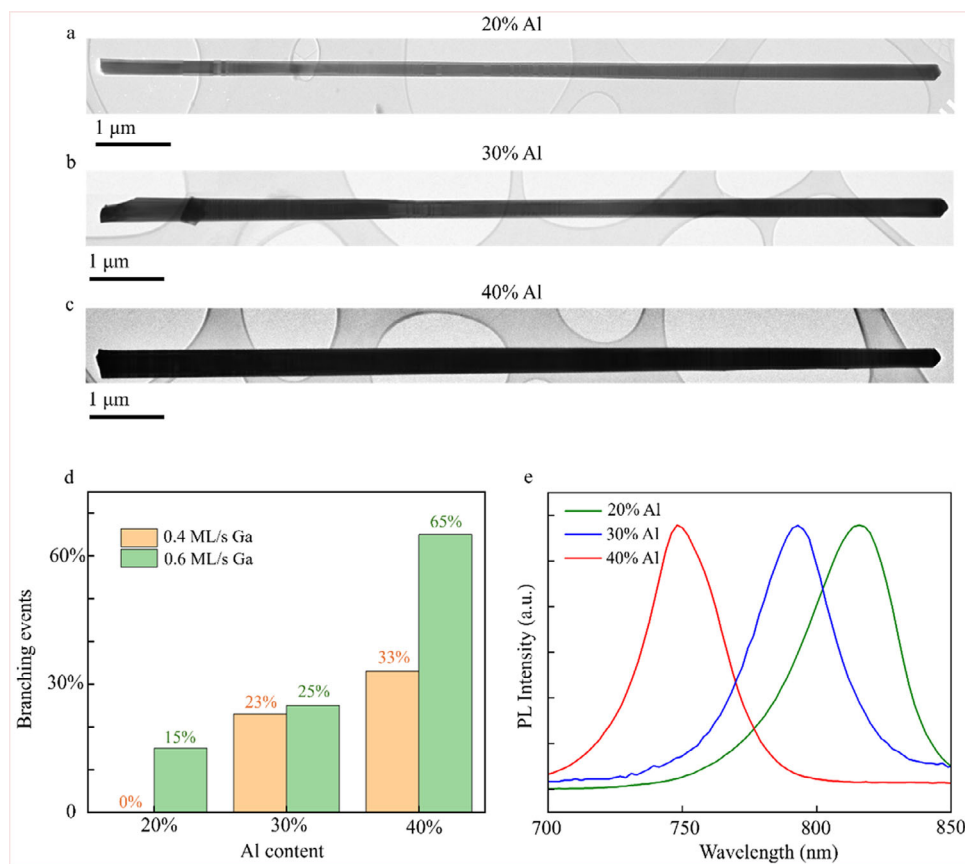


FIGURE 3 | a–c) Bright-field images showing representative examples of AlGaAs NWs with 20%, 30% and 40% nominal Al content, respectively. Increasing Al composition leads to some branching events; however, most of the NWs remain branchless, as observed in Figure 4b,c. d) Histogram showing the percentage of branching events as a function of the Al content for the current work (orange) and our previously published work (green). e) Room temperature photoluminescence spectra of the NW ensembles, confirming the increased incorporation of Al in the structures.

the challenging case of 40% Al-containing NWs. Out of the 15 individual NWs studied for each sample, no branches were observed for NWs with 20% nominal Al content, whereas in the case of the sample with 30% nominal Al content, just 3 NWs with branches were found. In the case of 40% nominal Al composition, 5 out of the 15 individual NWs exhibit small branches. This contrasts with earlier work, i.e., without the current optimization procedure, where multiple, long branches were formed in all samples [33, 34]. Further BF-TEM images of the 15 studied NWs from each sample are provided in Section 3 of the ESM. The results of a statistical analysis of the current NWs are shown in orange in the histogram of Figure 3d. For comparison, the same statistics for the unoptimized growth conditions based on our previous work are shown in green. In the latter case, the percentage of branched NWs is significantly higher, especially in the case of high Al-containing structures, where most of the NWs exhibited pronounced branching. This demonstrates the effectiveness of the current optimization procedure in achieving branchless AlGaAs NWs with increased Al content. TEM analysis and the BF images of Figure 3a–c and ESM Section show that tapering of the optimized NWs is small, indicating good uniformity, as required for implementation in many device applications.

The stated Al composition values of 20%, 30% and 40% are nominal, indicating an average Al content in the NW. Nevertheless, the Al distribution is expected to be complex and is determined by

the short diffusion length of Al and its high sticking coefficient as opposed to Ga, leading to its segregation at the external NW facets [33, 34]. Moreover, the different levels of elemental segregation in WZ and ZB regions, along with the polytypic nature and high density of rotational twins that are observed in such structures, further increase the complexity of a quantification of the Al distribution.

To study the incorporation of Al in the NWs, photoluminescence (PL) measurements were performed on the NW ensemble to determine the presence of Al in the NWs. The results are shown in Figure 3e, where a clear blueshift of the emission wavelength with increasing Al content is observed. This unambiguously demonstrates the higher incorporation of Al in samples with increasing nominal compositions of 20%, 30% and 40%, respectively. Further confirmation is provided from an analysis of the compositional profile of these NW samples determined via energy dispersive X-ray spectroscopy (EDX) examination. The resulting spectra are presented in Section 4 of the ESM.

The controllability of the AlGaAs NW synthesis that was demonstrated above is key to the functionality of the structures for device implementation. In the past, it has already been shown that deterministic regulation of the morphology or structure of III-V NWs has improved device performance. For instance, increasing the diameter of GaAsSb NWs has improved the

responsivity of NW-based photodetectors in the visible and near-infrared range [36], while high purity in GaAs NWs has greatly enhanced photodetector performance in terms of responsivity and detectivity [37]. Moreover, controlling the morphology of III-V NWs has been considered important in the fabrication of hybrid nanostructures, such as nanowire-quantum wells and NWQDs.

More specifically, a potential application arising from the manufacturing of branchless AlGaAs NWs with increased Al content is as a host for GaAs nanostructures, where AlGaAs with a high Al content provides strong carrier confinement. For example, as a result of their 0D nature, QDs are ideal elements for non-classical light emission with important functionality including single photon generation, which is crucial in quantum information processing [38, 39]. QDs grown via the widely adopted Stranski–Krastanov (SK) mode have restrictions in terms of controllability of the shape, size, and position, and the lattice parameters of the combined materials, as SK is a strain-driven process. In contrast, the axial MBE growth of QDs in NWs allows for the selective spatial positioning of the QD segment, where the NW acts as a waveguide for the light emission generated by the dot. NWQDs have emerged as promising candidates for LEDs [40], single photon sources [41, 42], and entangled photon emission [43]. In addition, multiple QDs embedded in NWs have shown promising potential for lasing, exploiting the 0D electronic properties of the dots and the natural cavity provided by the NW geometry [44–46]. Besides, controlling the dimensionality of III-V NWs has been proven to be a significant factor in a range of optoelectronic applications, including photodetector performance. A paradigm of such a function is the improved functionality shown by increasing the diameter

A short, 12 nm, GaAs segment was added to an AlGaAs NW with a nominal 40% Al composition. A schematic representation of the structure is shown in Figure 4a, with the AlGaAs in dark blue, the GaAs stem and segment in light blue, and the GaAs cladding layer in turquoise. The GaAs cladding layer has a thickness of 10 nm and serves a two fold role: first, it protects the AlGaAs NW from oxidation, and second, it leads to a reduction of carrier trapping at the dense AlGaAs surface states by acting as a passivation layer. It is interesting to underline that even though the existence of the short GaAs embedded segment was unambiguously confirmed via the optical analysis that will be discussed in the following paragraphs, it was further supported and substantiated by TEM analysis. The relevant results are presented in Section 5 of ESM.

The AlGaAs NWs containing a single GaAs segment were optically excited in a micro-photoluminescence (μ PL) system at 6K using a 450 nm continuous wave laser as the excitation source. The NWs were mechanically removed from the growth substrate and transferred to a new Si substrate with a SiO_2 surface layer. The transferred NWs are oriented horizontally on the new substrate. Figure 4b shows spectra recorded at regular steps of the laser position along the length of a typical NW, with two emission bands being present. The emission at 1.65 eV (752 nm) is observed along the full length of the NW, although it is weaker close to one end, probably reflecting the loss of carriers to the broken end. This peak is attributed to the AlGaAs barrier. The second peak is located at the lower energy level of 1.51 eV (821 nm) and is only observed for a limited range of laser positions. This latter peak

is ascribed to emission from the short GaAs segment. Figure 4c plots the intensity of the GaAs emission as a function of laser excitation position, clearly demonstrating its spatial localization in the central NW region. The full width at half maximum is 3 μm . This width will result from a convolution of the physical size of the GaAs segment and the spot size of the focused laser, plus a contribution from diffusion of photoexcited carriers created in the AlGaAs region. The latter two contributions will be significantly larger than the physical size of the GaAs segment and hence together will determine the measured width.

The spectral width of the GaAs emission is found to increase with increasing laser power but has a minimum value of 25 meV at the lowest excitation power density used, 5 W cm^{-2} . At this power density, the average carrier occupancy of the GaAs segment is of order one, and hence state-filling effects will not be present. Under these conditions, a QD should exhibit a single sharp emission line due to excitonic carrier recombination [47, 48]. The persistence of broad emission down to low excitation levels is attributed to the influence of surface states on the NW sidewalls and their random occupancy during the acquisition time of the spectra, which is many seconds. Electric fields produced by charges trapped in surface states perturb the QD emission energy via the quantum confined Stark effect, leading to time fluctuations in the emission energy [49]. The current structure contains only a thin 10 nm GaAs cladding layer to protect the core from oxidation. This provides a relatively small physical separation between the QD and the surface states, further enhancing the impact of the latter. One potential solution for further optimization would be the use of a thick surface passivation layer of a material with a reduced density of surface states, for example AlGaInP. Such a study is outside the scope of the current article and will be examined in future work.

To determine the size of carrier localization within the GaAs segment, temperature-dependent spectra were recorded. The log of intensity is plotted against inverse temperature in Figure 4d. This data is fitted to the function of the following form:

$$I = \frac{I_0}{1 + A \exp(-E_a/kT)} \quad (1)$$

where I_0 , A , and E_a are fitting parameters, with the latter being the activation energy. The best fit to the experimental data is shown in Figure 4c and indicates an activation energy of 97 ± 3 meV. The physical origin of this activation energy is unclear. As will be discussed later on in the current manuscript, AlGaAs compositional distribution is expected to be non-uniform, hence the energies of the barrier states close to the GaAs segment cannot be accurately defined. GaAs NWs have been shown to exhibit polytypism with a mixed ZB/WZ phase, with transitions between these phases being possible. Despite the aforementioned uncertainty in the origin of the activation energy, its relatively large value demonstrates the potential of the current NWs to provide strong carrier confinement within embedded GaAs nanostructures, as required for the operation of novel light emitters at high temperatures.

The emission energy of the AlGaAs, 1.65 eV, is much lower than expected for an Al composition of 40%; instead, it is consistent with a much lower composition of 11% [50]. As discussed

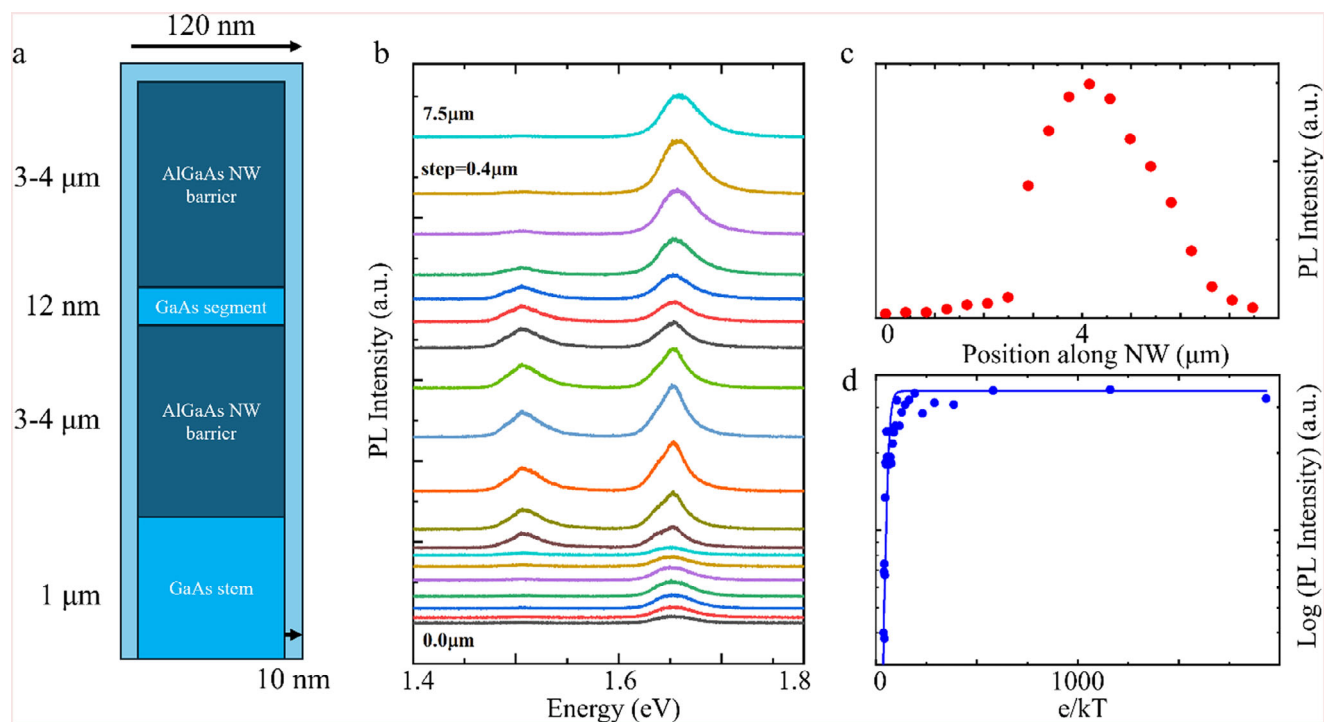


FIGURE 4 | a) Schematic representation of an AlGaAs NW with the GaAs segment. b) Position-dependent μ PL spectra of an AlGaAs NW with a GaAs segment showing two emission bands, the lower energy one being observed for excitation in the middle of the NW and hence attributed to the GaAs segment. c) GaAs emission intensity plotted as a function of the position of the excitation along the NW, confirming its spatial localization. d) Log of the intensity of the GaAs emission as a function of the inverse temperature, demonstrating a large activation energy of 97 ± 3 meV.

previously, this is attributed to a non-uniform Al composition and the diffusion of photo-excited carriers to regions of lower Al. The emission from the AlGaAs hence reflects spatially small regions of low Al composition in an inhomogeneous AlGaAs NW with a significantly higher average Al composition [34, 51]. This issue is discussed further below.

It is important to note that QD-like emission was observed from AlGaAs/GaAs NWQDs in our earlier work [33]. At low temperature, the GaAs emission exhibited a narrow linewidth and a strongly localized peak, which rapidly quenched above 60 K. These samples had a lower Al composition than in the current work; the low Al composition presented a relatively small potential barrier for carrier confinement, resulting in rapid quenching of the emission with increasing temperature. In the current work, the larger Al composition results in a much larger carrier confinement, with room temperature measurements showing spatially localized GaAs emission, as discussed below.

Additional optical measurements were performed at room temperature in a second μ PL system, which used a continuous wave, 532 nm laser as the excitation source. The excitation spot was centered on the GaAs so that carriers were photoexcited and recombined in both the AlGaAs and the GaAs segments. The excitation power was modified to reveal the underlying carrier recombination processes, with the results of the power-dependent μ PL shown in Figure 5a. Similar to the 6K measurements, though shifted by the temperature variation of the bandgaps, two clear peaks are observed at 1.465 eV (846 nm) and 1.67 eV (742 nm), with the low-energy peak attributed to emission from the GaAs segment, and the 1.67 eV emission from

the AlGaAs barriers. Figure 5b shows the integrated intensity normalized to the excitation power, a measure of the relative recombination efficiency, as a function of the power density. At excitation power densities $>100 \text{ W cm}^{-2}$, the GaAs segment intensity levels off and remains saturated up to the highest power density applied; this is in contrast to the AlGaAs intensity, which at high power increases super linearly with power. We propose that this saturation reflects the filling of QD-like states due to a reduced DOS, the result of full quantum confinement. The AlGaAs barriers have no quantum confinement and a higher DOS, resulting in minimal state filling; thus, the intensity does not saturate up to the highest applied power. The super-linear increase in intensity of the AlGaAs may result from the saturation of non-radiative defects with increasing power.

Further evidence for state filling is shown by the change in spectral shape with increasing excitation power in Figure 5a. At each power, the spectra were fitted using a Lasher-Stern-Wurfel model for band-to-band recombination [52], where only the Fermi energy (due to band-filling effects) and the emission intensity were allowed to vary with power. Figure 5c shows how the Fermi energy varies for both the GaAs segment and the barrier. The equations used for this analysis can be found in Section 6 of the ESM. We observe that the Fermi energy remains unaltered for the barrier-related emission, whereas signs of strong band-filling effects are observed for the GaAs emission on the low-energy side of the spectrum. This is in accordance with the clear blueshift of the GaAs emission with increasing excitation powers that can be seen in Figure 5a. There is hence evidence that the GaAs segment displays QD-like properties at room temperature. In agreement with the low temperature μ PL results

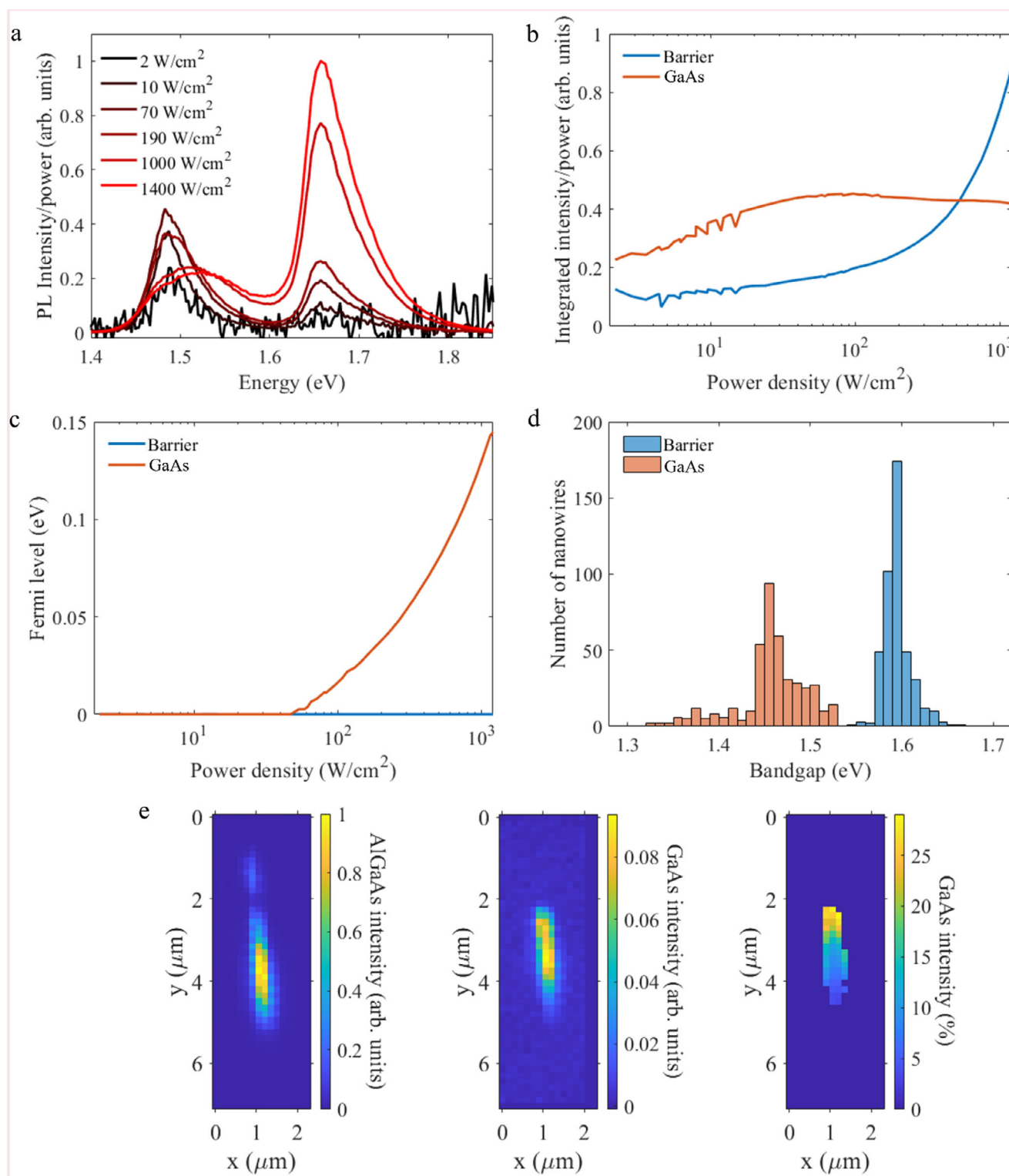


FIGURE 5 | a) Room temperature power-dependent μ PL spectra normalized to the excitation power showing two peaks, one at 1.465 eV (GaAs emission) and a second at 1.67 eV (AlGaAs barrier emission). b) The relative efficiencies of the GaAs and barrier emission (Intensity/Power) as a function of the incident laser power density, showing saturation of the GaAs emission. c) Fermi Energy level as a function of power density for both the GaAs and barrier emission, showing band-filling effects for the former, consistent with a QD-associated reduced density of states. d) Histogram statistics of 438 different individual AlGaAs/GaAs NW structures, showing the bandgap energy of the emission. e) Maps showing the intensity of the emission as a function of exciting laser position from the AlGaAs and GaAs segments and GaAs/AlGaAs normalized intensity, respectively.

discussed previously, the GaAs emission has a non-zero linewidth in the limit of very low excitation power densities (~ 60 meV). This indicates a contribution from other broadening processes in addition to state filling, for example, thermal broadening and random occupancy of surface states.

The AlGaAs emission energy at room temperature is located around 1.67 eV, the Al content this energy reflects is different from the nominal one. Specifically, an Al composition below 20% is determined, with the median value among the measured structures being 14%. This discrepancy has been observed in previous work for self-catalyzed AlGaAs/GaAs NWQDs [33], where it was concluded that the estimation of Al composition in the ternary alloy via μ PL measurements disagrees with the nominal value and also compositional measurements via energy dispersive X-ray spectroscopy (EDX). The consistent underestimation of the Al content based on μ PL can be explained due to its high sensitivity to small regions of narrower bandgap materials. For the details, please refer to the explanation given when commenting on Figure 4b above.

To probe inter-NW variations, high-throughput room temperature μ PL was used to measure the luminescence of 438 individual NWs at a fixed laser power. Each measured spectrum was fitted using a Lasher-Stern-Wurfel model, allowing the bandgap to be extracted. More information on this approach can be found in Ref. [53]. The emission energy of the GaAs segment extends from 1.38 to 1.52 eV (815–898 nm). The AlGaAs barrier emission is centered around 1.6 eV. The NW-to-NW variation of the GaAs emission likely stems from variations in the dot size—both lateral and radial—among the individual structures. A contribution from the effect of charges trapped in surface states may also contribute, and this would explain why the GaAs segment emission can occur below the bulk GaAs bandgap. It is interesting to underline that the precise structure of the GaAs segment is unknown. We note that the presence of both ZB and WZ phases can lead to the formation of a type-II band structure, resulting in a reduction of the emission energy [54]. In contrast, differences in the bandgap energy of the AlGaAs barrier derive from compositional variation, which is anticipated based on previous AlGaAs NW studies [33, 34]. The histogram for the emission energies is presented in Figure 5d.

To assess whether the GaAs emission is spatially localized at room temperature, a high-resolution PL map was measured for a representative NW. In these measurements, the PL intensity is measured as a function of the position of the exciting laser spot. The intensity of the AlGaAs and GaAs emission, as well as their ratio, is shown in Figure 5e. As expected, the AlGaAs emission is observed for excitation over a large length of the NW, except for a low-intensity “gap” at a y value of 2 μ m, associated with the GaAs segment. The GaAs emission is also observed for excitation over a wide area, attributed to diffusion and capture of carriers excited in the AlGaAs by the lower bandgap GaAs. The limited spatial extent of the GaAs emission can be more easily seen by plotting the GaAs emission intensity as a percentage of the total emission intensity, $I(\text{GaAs})/(I(\text{GaAs})+I(\text{AlGaAs}))\times 100\%$, in Figure 5e. This shows that excitation at the y value of 2 μ m results in emission dominated by the GaAs; this is the expected axial location of the GaAs segment in the NW.

The optical study presented above demonstrates that localized emission from the GaAs segment has been achieved. This emission exhibited some properties consistent with those expected for a QD at both 6K and at room temperature. However, the GaAs segment remains relatively large, particularly in the radial direction, and a significantly smaller size is required to display the full QD properties required for applications such as single photon emission. This is because the production of single photons requires spectrally separable exciton and biexciton emission, typically observed when the dot dimensions are 10 nm or below. Hence, further work is imperative to reduce the NW diameter dimensions and optimize the surface passivation layer to eventually obtain hybrid structures that can be functional for a plethora of device applications.

It is important to note that one factor that plays a key role in the optoelectronic performance of the structures is the elemental composition and distribution. As discussed earlier, one of the fundamental advantages of ternary III-V NWs is the capability of bandgap modulation, hence emission wavelength, based on the compositional distribution [3]. In previous works, we have demonstrated the intricacy of the Al distribution, which presents a high degree of interest but also leads to considerable challenges in the optoelectronic results. Specifically, Al tends to adhere to the sidewall facets, leading to the spontaneous formation of an Al-rich AlGaAs shell [33, 34], while the short diffusion length of Al leads to its preferential segregation at the bottom part of the NW, causing a gradient of the composition, with the top part being Al-deficient [28, 33, 34]. The same observations have been made in the current work, as described in the ESM (Section 4). Besides, the tendency of Al to be easily oxidized can lead to the formation of additional trap states due to the oxygen-induced chemical bonds that lead to atomic reconstruction, which can reduce radiative recombination lifetime. This can usually be circumvented via the synthesis of a passivation shell, as previously reported by our group in the case of ultrathin InP shell surrounding InAsP NW cores, which led to a three fold increase in radiative recombination lifetime and a reduction of surface recombination velocity by a factor of 0.7 [55]. Due to the high level of oxidation of Al, the formation of a GaAs shell in the current work was imperative in order to achieve better optical performance, which can be shown via the sustainable GaAs emission up to room temperature.

3 | Conclusion

In conclusion, we report the self-catalyzed synthesis of AlGaAs NWs via MBE with a significant reduction in the occurrence of the previously frequently observed self-formed branches, whilst maintaining minimal NW tapering and using elevated Al content. Such structures will find application in non-classical light-emitting applications. Samples were grown with varying Ga growth rate, Al composition, and V/III ratio, and were studied by SEM to determine the optimal growth parameters. TEM analysis confirmed a predominantly ZB crystal phase, with WZ insertions and a high density of stacking faults. Branching events remain low even for challenging Al-rich growth conditions, indicating the synergic influence of group III elemental supply in NW growth and confirming the controllability of branch nucleation via growth parameter modulation. Nominal 40% Al-containing

AlGaAs NWs grown using the optimized growth parameters were selected for the embedding of a single short GaAs segment. Spatially localized emission at both 6 K and room temperature was observed from this segment, with state-filling behavior observed at room temperature, indicating QD-like properties. The use of a high Al content NW provides strong carrier confinement, with a large activation energy observed for quenching of the GaAs emission, a requirement for devices operating at elevated temperatures. Our work contributes to the understanding and optimization of the technologically important AlGaAs NWs and AlGaAs NWs with GaAs nanostructures, with potential for light-emitting applications, including NWQW micro-lasers and NWQDs for single photon generation.

4 | Growth Methods

NWs were grown in a Veeco GEN 930 solid-source MBE system. Al and Ga solid sources were used for group III elements, while an As solid source with a cracker was used for the group V element. The growth was performed on 4° offcut Si (111) wafers, which were initially deoxidized and then left in an ambient environment for 24 h, for a uniform native oxide layer to form. Subsequently, the substrates were degassed in the preparation chamber via thermal annealing at 600°C for 60 min. The growth started with Ga deposition for 5 min to form the Ga droplets, with the chosen Ga flux during this step corresponding to the thin film growth rate of 0.3 ML/s. This was followed by the growth of 1 µm-long GaAs stems at 610°C. Next, Al was supplied for the synthesis of AlGaAs NWs. The Ga and Al fluxes used in our growth were expected to produce $\text{Al}_x\text{Ga}_{1-x}\text{As}$ thin films of the same composition on GaAs (001) substrates. The growth continued for 100 min for all samples and was continuous, so that all developed branches were self-formed. For the NW with a GaAs segment, the growth conditions were identical to the ones used for the synthesis of branchless AlGaAs NWs with 40% Al composition. After growth of half of the NW length, the Al supply was interrupted for 7 s to form the GaAs QD segment. Then Al was reintroduced to form the top half of the AlGaAs NW and to fully encapsulate the GaAs dot in the central region of the AlGaAs NW. Following the NW synthesis, the Al and Ga shutters were closed, and the droplet was crystallized for 5 min under a high As flux. The temperature was then lowered to 510°C and Ga was reintroduced in the reactor for 5 min, to promote vapor-solid lateral growth of a 10 nm-thick GaAs shell. The GaAs cladding layer provides surface passivation and protects the AlGaAs NW from oxidation.

5 | Structural Studies

The morphology of the structures was studied using Scanning Electron Microscopy (SEM), performed using a Zeiss CrossBeam XB 1540 system. The samples were tilted by 30°, and the voltage of the electron beam was kept at 20 kV. Additional structural characterization of the AlGaAs NWs was conducted via Transmission Electron Microscopy (TEM). NWs were transferred to holey carbon grids and studied using a doubly corrected ARM200F microscope, operating at 200 kV.

6 | Optical Measurements

Room-temperature PL measurements of NW ensembles were conducted using a Nanometrics RPM2000 machine using a 532 nm laser source.

Low-temperature μPL spectra were obtained from single NWs, which had been removed from the original substrate and transferred to a new Si wafer. μPL spectra were excited by a cw 450 nm diode laser. The samples were measured under vacuum inside a continuous flow cryostat (base temperature 6 K). The incident laser was focused with a 20x long working distance microscope objective to a spot size of ~ 1 µm diameter. The resultant PL was collected by the same microscope objective and focused into a 0.75 m spectrometer, where the spectral components were resolved and detected using a 300 L/mm grating and a nitrogen-cooled Si CCD.

The room temperature μPL measurements were performed using an optical confocal microscope, which is described further in ref [51]. A 532 nm continuous wave laser was used as the excitation source for the power-dependent PL, the high-throughput PL, and the high-resolution PL maps. In each case, the optics were changed to suit the experiment.

For power-dependent PL, the laser was focused using a 20x magnification objective lens to a spot diameter of 1.4 µm, centered on the GaAs segment. The excitation power was varied between 0.02 and 20 µW using a motorized variable ND filter wheel, and the luminescence of the NW was collected using a back-scattered arrangement through the same objective lens. The light from a 5 µm diameter spot, also centered on the GaAs segment, was coupled into an optical fiber, and the spectrum was measured using a calibrated Horiba iHR550 spectrometer with a minimum resolution of 1 nm.

For the high-throughput PL, the 20x objective was used, with a laser power of 0.2 µW. This was sufficient to avoid band-filling effects in the QD, and the excitation was centered on the QD in each NW. NWs were automatically located on the substrate using optical imaging and machine vision, and the PL spectrum was measured using the same hardware that was used for the power dependence.

For the high-resolution maps, a 100x objective was used, with an excitation spot diameter of ~ 600 nm, and a laser power of 20 µW. The light from a 1 µm spot, centered on the excitation spot, was collected into a fiber and coupled to the spectrometer, as before. Mapping was performed by translating the sample in x-y with a step size of 0.15 µm over an 8 by 8 µm area.

Acknowledgements

The authors acknowledge the support of the UK Engineering and Physical Sciences Research Council-EPSC (Grant Numbers: EP/V028596/1, EP/W002752/1, EP/W002302/1, and EP/W002418/1) and the EPSC National Epitaxy Facility. Patrick Parkinson acknowledges funding under the UKRI Future Leaders Fellowship programme (MR/T021519/1).

Conflicts of Interest

The authors declare no conflicts of interest.

Data Availability Statement

Research data are not shared.

References

1. T. Martensson, P. T. Svensson, B. A. Wacaser, et al., "Epitaxial III–V Nanowires on Silicon," *Epitaxial III–V Nanowires on Silicon* 4, no. 10 (2004): 1987–1990.
2. M. Heiss, E. Russo-Averchi, A. Dalmau-Mallorqui, et al., "III–V Nanowire Arrays: Growth and Light Interaction," *III–V Nanowire Arrays: Growth and Light Interaction* 25 (2014): 014015.
3. G. Boras, X. Yu, and H. Liu, "III–V Ternary Nanowires on Si Substrates: Growth, Characterization and Device Applications," *Journal of Semiconductors* 40 (2019): 101301, <https://doi.org/10.1088/1674-4926/40/10/101301>.
4. V. G. Dubrovskii and E. D. Leshchenko, "Kinetically Controlled Composition of III–V Ternary Nanostructures," *Physical Review Materials* 7 (2023): 056001, <https://doi.org/10.1103/PhysRevMaterials.7.056001>.
5. M. J. Tambe, S. K. Lim, M. J. Smith, L. F. Allard, and S. Gradečak, "Realization of Defect-free Epitaxial Core-shell GaAs/AlGaAs Nanowire Heterostructures," *Applied Physics Letters* 93 (2008): 151917, <https://doi.org/10.1063/1.3002299>.
6. G. Koblmüller, B. Mayer, T. Stettner, G. Abstreiter, and J. J. Finley, "GaAs–AlGaAs Core–Shell Nanowire Lasers on Silicon: Invited Review," *Semiconductor Science and Technology* 32 (2017): 053001, <https://doi.org/10.1088/1361-6641/aa5e45>.
7. D. Saxena, S. Mokkapatil, P. Parkinson, et al., "Optically Pumped Room-Temperature GaAs Nanowire Lasers," *Nature Photonics* 7, no. 7 (2013): 963–968, <https://doi.org/10.1038/nphoton.2013.303>.
8. T. Stettner, P. Zimmermann, B. Loitsch, et al., "Coaxial GaAs–AlGaAs Core-multishell Nanowire Lasers With Epitaxial Gain Control," *Applied Physics Letters* 108 (2016): 011108, <https://doi.org/10.1063/1.4939549>.
9. K. Tomioka, J. Motohisa, S. Hara, K. Hiruma, and T. Fukui, "GaAs/AlGaAs Core Multishell Nanowire-Based Light-Emitting Diodes on Si," *Nano Letters* 10, no. 5 (2010): 1639–1644, <https://doi.org/10.1021/nl9041774>.
10. B. Romeira, J. Borme, H. Fonseca, J. Gaspar, and J. B. Nieder, "Efficient Light Extraction in Subwavelength GaAs/AlGaAs Nanopillars for Nanoscale Light-emitting Devices," *Optics Express* 28, no. 22 (2020): 32302–32315, <https://doi.org/10.1364/OE.402887>.
11. X. Dai, S. Zhang, Z. Wang, et al., *GaAs/AlGaAs Nanowire Photodetector* 14, no. 5 (2014): 2688–2693.
12. X. Zhu, F. Lin, Z. Zhang, et al., "Enhancing Performance of a GaAs/AlGaAs/GaAs Nanowire Photodetector Based on the Two-Dimensional Electron–Hole Tube Structure," *Nano Letters* 20, no. 4 (2020): 2654–2659, <https://doi.org/10.1021/acs.nanolett.0c00232>.
13. Y. Yu, X. M. Dou, B. Wei, et al., "Self-Assembled Quantum Dot Structures in a Hexagonal Nanowire for Quantum Photonics," *Advanced Materials* 26, no. 17 (2014): 2710–2717, <https://doi.org/10.1002/adma.201304501>.
14. M. Heiss, Y. Fontana, A. Gustafsson, et al., "Self-assembled Quantum Dots in a Nanowire System for Quantum Photonics," *Nature Materials* 12 (2013): 439–444, <https://doi.org/10.1038/nmat3557>.
15. N. Jeon, B. Loitsch, S. Morkötter, et al., "Alloy Fluctuations Act As Quantum Dot-like Emitters in GaAs–AlGaAs Core–Shell Nanowires," *ACS Nano* 9, no. 8 (2015): 8335–8343.
16. N. Erhard, S. Zenger, S. Morkötter, et al., "Ultrafast Photodetection in the Quantum Wells of Single AlGaAs/GaAs-Based Nanowires," *Nano Letters* 15 (2015): 6869, <https://doi.org/10.1021/acs.nanolett.5b02766>.
17. M. De La Mata, X. Zhou, F. Furtmayr, et al., "A Review of MBE Grown 0D, 1D and 2D Quantum Structures in a Nanowire," *Journal of Materials Chemistry C* 1 (2013): 4300.
18. M. Fickenscher, T. Shi, H. E. Jackson, et al., "Structural, and Numerical Investigations of GaAs/AlGaAs Core-Multishell Nanowire Quantum Well Tubes," 13 (2013): 1016.
19. V. N. Kats, V. P. Kocheresko, A. V. Platonov, et al., "Optical Study of GaAs Quantum Dots Embedded Into AlGaAs Nanowires," *Semiconductor Science and Technology* 27 (2012): 015009, <https://doi.org/10.1088/0268-1242/27/1/015009>.
20. G. E. Cirlin, R. R. Reznik, I. V. Shtrom, et al., "Hybrid GaAs/AlGaAs Nanowire—Quantum dot System for Single Photon Sources," *Semiconductors (Translation of Fizika I Tekhnika Poluprovodnikov (Sankt-Peterburg))* 52 (2018): 462, <https://doi.org/10.1134/S1063782618040103>.
21. V. P. Kochereshko, V. N. Kats, A. V. Platonov, et al., "GaAs Single Quantum Dot Embedded Into AlGaAs Nanowire," *AIP Conference Proceeding* 1566 (2013): 482.
22. D. Baretin, I. V. Shtrom, R. R. Reznik, and G. E. Cirlin, "Model of a GaAs Quantum Dot in a Direct Band Gap AlGaAs Wurtzite Nanowire," *Nanomaterials* 13, no. 11 (2023): 1737, <https://doi.org/10.3390/nano13111737>.
23. Z. H. Wu, M. Sun, X. Y. Mei, and H. E. Ruda, "Growth and Photoluminescence Characteristics of AlGaAs Nanowires," *Applied Physics Letters* 85 (2004): 657–659.
24. V. N. Kats, V. P. Kocheresko, A. V. Platonov, et al., "Optical Study of GaAs Quantum Dots Embedded Into AlGaAs Nanowires," *Semiconductor Science and Technology* 27 (2012): 015009, <https://doi.org/10.1088/0268-1242/27/1/015009>.
25. C. Chen, S. Shehata, C. Fradin, R. LaPierre, C. Couteau, and G. Weihs, "Self-Directed Growth of AlGaAs Core–Shell Nanowires for Visible Light Applications," *Nano Letters* 7 (2007): 2584, <https://doi.org/10.1021/nl070874k>.
26. S. K. Lim, M. J. Tambe, M. M. Brewster, and S. Gradečak, "Controlled Growth of Ternary Alloy Nanowires Using Metalorganic Chemical Vapor Deposition," *Nano Letters* 8 (2008): 1386, <https://doi.org/10.1021/nl080129n>.
27. A. Li, D. Ercolani, L. Lugani, et al., "Synthesis of AlAs and AlAs–GaAs Core–Shell Nanowires," *Crystal Growth & Design* 11 (2011): 4053–4058.
28. V. G. Dubrovskii, I. V. Shtrom, R. R. Reznik, et al., "Origin of Spontaneous Core–Shell AlGaAs Nanowires Grown by Molecular Beam Epitaxy," *Crystal Growth & Design* 16, no. 12 (2016): 7251–7255, <https://doi.org/10.1021/acs.cgd.6b01412>.
29. N. Gregersen, T. R. Nielsen, J. Claudon, J.-M. Gerard, and J. Mork, "Controlling the Emission Profile of a Nanowire With a Conical Taper," *Optics Letters* 33, no. 15 (2008): 1693–1695, <https://doi.org/10.1364/OL.33.001693>.
30. K. A. Dick and P. Caroff, "Metal-Seeded Growth of III–V Semiconductor Nanowires: Towards Gold-Free Synthesis," *Nanoscale* 6 (2014): 3006, <https://doi.org/10.1039/C3NR06692D>.
31. S. Breuer, C. Pfüller, T. Flissikowski, et al., "Suitability of Au- and Self-Assisted GaAs Nanowires for Optoelectronic Applications," *Nano Letters* 11 (2011): 1276, <https://doi.org/10.1021/nl104316t>.
32. S. Perera, M. A. Fickenscher, H. E. Jackson, et al., "Nearly Intrinsic Exciton Lifetimes in Single Twin-Free GaAs/AlGaAs Core–Shell Nanowire Heterostructures," *Applied Physics Letters* 93 (2008): 053110, <https://doi.org/10.1063/1.2967877>.
33. G. Boras, X. Yu, H. A. Fonseca, et al., "Self-Catalyzed AlGaAs Nanowires and AlGaAs/GaAs Nanowire–Quantum Dots on Si Substrates," *The Journal of Physical Chemistry C* 125, no. 26 (2021): 14338–14347, <https://doi.org/10.1021/acs.jpcc.1c03680>.

34. G. Boras, X. Yu, H. A. Fonseka, et al., "Checked Patterned Elemental Distribution in AlGaAs Nanowire Branches via Vapor-Liquid-Solid Growth," *Nanoscale* 12 (2020): 15711–15720, <https://doi.org/10.1039/D0NR02577A>.
35. C. Cheng and H. J. Fan, "Branched Nanowires: Synthesis and Energy Applications," *Nano Today* 7, no. 4 (2012): 327–343, <https://doi.org/10.1016/j.nantod.2012.06.002>.
36. Y. Kang, X. Hou, Z. Zhang, et al., "Ultrahigh-Performance and Broadband Photodetector From Visible to Shortwave Infrared Band Based on GaAsSb Nanowires," *Chemical Engineering Journal* 501 (2024): 157392, <https://doi.org/10.1016/j.cej.2024.157392>.
37. Y. Kang, X. Hou, Z. Zhang, et al., "Enhanced Visible-NIR Dual-Band Performance of GaAs Nanowire Photodetectors Through Phase Manipulation," *Advanced Optical Materials* 13 (2025): 2500289, <https://doi.org/10.1002/adom.202500289>.
38. B.-C. Ren and F.-G. Deng, "Hyper-Parallel Photonic Quantum Computation With Coupled Quantum Dots," *Scientific Reports* 4 (2015): 4623, <https://doi.org/10.1038/srep04623>.
39. D. C. Unitt, A. J. Bennett, P. Atkinson, et al., "Quantum Dots as Single-photon Sources for Quantum Information Processing," *Journal of Optics B: Quantum and Semiclassical Optics* 7 (2005): S129–S134, <https://doi.org/10.1088/1464-4266/7/7/001>.
40. E. D. Minot, F. Kelkensberg, M. van Kouwen, et al., "Single Quantum Dot Nanowire LEDs," *Nano Letters* 7, no. 2 (2007): 367–371.
41. P. Yu, Z. Li, T. Wu, et al., "Nanowire Quantum Dot Surface Engineering for High Temperature Single Photon Emission," *ACS Nano* 13, no. 11 (2019): 1349213500.
42. M. N. Makhonin, A. P. Foster, A. B. Krysa, et al., "Homogeneous Array of Nanowire-Embedded Quantum Light Emitters," *Nano Letters* 13, no. 3 (2013): 861–865, <https://doi.org/10.1021/nl303075q>.
43. M. A. M. Versteegh, M. E. Reimer, K. D. Jöns, et al., "Observation of Strongly Entangled Photon Pairs From a Nanowire Quantum Dot," *Nature Communications* 5 (2014): 5298, <https://doi.org/10.1038/ncomms6298>.
44. J. Tatebayashi, S. Kako, J. Ho, Y. Ota, S. Iwamoto, and Y. Arakawa, "Room-temperature Lasing in a Single Nanowire With Quantum Dots," *Nature Photonics* 9 (2015): 501–505, <https://doi.org/10.1038/nphoton.2015.111>.
45. J. Ho, J. Tatebayashi, S. Sergent, et al., "A Nanowire-Based Plasmonic Quantum Dot Laser," *Nano Letters* 16, no. 4 (2016): 2845–2850, <https://doi.org/10.1021/acs.nanolett.6b00706>.
46. J. Tatebayashi, Y. Ota, S. Ishida, M. Nishioka, S. Iwamoto, et al., "Nanowire-Quantum-Dot Lasers On Flexible Membranes," *Applied Physics Express* 11 (2018): 065002.
47. J. Tatebayashi, Y. Ota, S. Ishida, M. Nishioka, S. Iwamoto, and Y. Arakawa, "Optical Properties of Site-Controlled InGaAs Quantum Dots Embedded in GaAs Nanowires By Selective Metalorganic Chemical Vapor Deposition," *Japanese Journal of Applied Physics* 51 (2012): 11PE13.
48. Y. Zhang, A. V. Velichko, H. A. Fonseka, et al., "Defect-Free Axially Stacked GaAs/GaAsP Nanowire Quantum Dots with Strong Carrier Confinement," *Nano Letters* 21, no. 13 (2021): 5722–5729.
49. A. Berthelot, I. Favero, G. Cassaboïs, et al., "Unconventional Motional Narrowing in the Optical Spectrum of a Semiconductor Quantum Dot," *Nature Physics* 2 (2006): 759–764, <https://doi.org/10.1038/nphys433>.
50. A. J. Ekpunobi and A. O. E. Animalu, "Band Offsets and Properties of AlGaAs/GaAs and AlGaIn/GaN Material Systems," *Superlattices and Microstructures* 31, no. 5 (2002): 247–252, <https://doi.org/10.1006/spmi.2002.1042>.
51. H. A. Fonseka, A. V. Velichko, Y. Zhang, et al., "Self-Formed Quantum Wires and Dots in GaAsP-GaAsP Core-Shell Nanowires," *Nano Letters* 19, no. 6 (2019): 4158–4165.
52. S. A. Church, N. Patel, R. Al-Abri, et al., "Holistic Nanowire Laser Characterization as a Route to Optimal Design," *Advanced Optical Materials* 11, no. 7 (2023): 2202476, <https://doi.org/10.1002/adom.202202476>.
53. S. A. Church, F. Vitale, A. Gopakumar, et al., "Data-Driven Discovery for Robust Optimization of Semiconductor Nanowire Lasers," *Laser & Photonics Reviews* 19, no. 3 (2025): 2401194.
54. D. Spirkoska, J. Arbiol, A. Gustafsson, et al., "Structural and Optical Properties of High Quality Zinc-Blende/Wurtzite GaAs Nanowire Heterostructures," *Physical Review B* 80 (2009): 245325, <https://doi.org/10.1103/PhysRevB.80.245325>.
55. L. Chen, S. O. Adeyemo, A. H. Fonseka, et al., "Long-Term Stability and Optoelectronic Performance Enhancement of InAsP Nanowires With an Ultrathin InP Passivation Layer," *Nano Letters* 22, no. 8 (2022): 3433–3439, <https://doi.org/10.1021/acs.nanolett.2c00805>.

Supporting Information

Additional supporting information can be found online in the Supporting Information section.

Supporting file: admi70331-sup-0001-SuppMat.docx